



Thermal Large-Eddy Simulations methods to model highly anisothermal and turbulent flows

Martin David, Adrien Toutant, Françoise Bataille

► To cite this version:

Martin David, Adrien Toutant, Françoise Bataille. Thermal Large-Eddy Simulations methods to model highly anisothermal and turbulent flows. *Physics of Fluids*, 2023, 10.1063/5.0139433 . hal-04002588v2

HAL Id: hal-04002588

<https://hal.science/hal-04002588v2>

Submitted on 6 Mar 2023

HAL is a multi-disciplinary open access archive for the deposit and dissemination of scientific research documents, whether they are published or not. The documents may come from teaching and research institutions in France or abroad, or from public or private research centers.

L'archive ouverte pluridisciplinaire **HAL**, est destinée au dépôt et à la diffusion de documents scientifiques de niveau recherche, publiés ou non, émanant des établissements d'enseignement et de recherche français ou étrangers, des laboratoires publics ou privés.

T-LES methods to model highly anisothermal and turbulent flows

Thermal Large-Eddy Simulations methods to model highly anisothermal and turbulent flows

M. David,^{a)} A. Toutant,^{b)} and F. Bataille^{c)}

PROMES-CNRS laboratory (UPR 8521), Université de Perpignan via Domitia, Technosud-Rambla de la thermodynamique, 66100 Perpignan, France

(Dated: 7 February 2023)

Thermal Large-Eddy Simulations (T-LES) of highly anisothermal and turbulent channel flows are assessed using Direct Numerical Simulations (DNS). The investigated conditions are representative of solar receivers used in concentrated solar power towers. Four thermal operating conditions are considered. They aim to study several locations in the solar receiver. They are distinguished by different temperature profiles and thus different wall heat fluxes. The mean friction Reynolds number is close to 800 for all the simulations. The Navier-Stokes equations are solved under the low Mach number approximation. The nonlinear terms corresponding to the velocity-velocity and the velocity-temperature correlations are modeled. Functional, structural, and mixed models are investigated. An extension of the Anisotropic Minimum Dissipation (AMD) model to compressible case and two-layer mixed models are proposed and assessed. Fourth-order and second-order centered schemes are tested for the discretization of the momentum convection term. Firstly, a global assessment of 16 T-LES approaches on mean quantities and correlations for three different meshes is performed in reference conditions. Then, three of the T-LES are selected for more detailed analyzes. The mesh effect and the influence of the thermal conditions on the model accuracy are investigated. These detailed studies consist of the comparison of the relative error of the T-LES on mean quantities and correlations and the visualization of the normalized profiles as functions of the wall-normal distance. The results highlight the good agreement of two-layer mixed models consisting in the combination of the Bardina and the AMD models with the DNS for the three tested meshes.

I. INTRODUCTION

Gas-pressurized solar receivers are several meters long and are characterized by strong asymmetrical heating of the heat transfer fluid and intense turbulence¹. Finding analytical solution of the problem is currently not possible due to mathematical complexities and no statistical closure methods can be utilized effectively due to its lack of information and their unfaithful representation of the dynamics. For that reason, numerical simulation of solar receivers are needed^{2,3}. The Direct Numerical Simulation (DNS) of the system is too costly due to the absorber size and the operating conditions. By modeling the smallest turbulence scales, Large Eddy Simulation (LES) permits significantly reducing the computational cost when compared to a DNS in which all length and time scales must be resolved, all the way down to the Kolmogorov length scale. The LES approach allows to compute part of the receiver and investigate more complex geometries to enhance heat transfer from the concentrated sunlight to the fluid.

The extreme operating conditions encountered in solar receivers make the flow difficult to approximate with a numerical model. Particularly, the strong anisotropy of the fluid dynamic make the flow computation complex. Similar physical behaviors can be observed in turbulent flows induced by Rayleigh-Taylor and Richtmyer-Meshkov instabilities^{4–8} or in rotating stratified turbulence⁹. In the studied case, the high-temperature gradients require to take into account the term

related to the velocity-temperature correlation¹⁰. The following papers investigate tensorial subgrid-scale heat flux models. Peng and Davidson¹¹ propose a model which accounts for the subgrid-scale (SGS) heat flux in terms of the large-scale strain-rate tensor and the temperature gradients. Contrary to the linear isotropic eddy diffusivity models, this approach is equivalent to using a tensor diffusivity. However, the local dissipation introduced by this model can take negative values. As a consequence, it produces a finite-time blow-up and thus cannot be used as a standalone SGS heat flux model. The same drawback appears when using the nonlinear Leonard model, which is the leading term of the Taylor series of the SGS heat flux. To overcome these instability issues, Higgins *et al.*¹² investigate a mixed model for SGS heat flux that is composed of the Leonard¹³ and the Smagorinsky¹⁴ models. Wang *et al.*¹⁵ use the most general explicit algebraic formulations possible to construct the family of SGS heat flux models. In their study, as in Ref.¹¹ the model accounts for the SGS heat flux in terms of the resolved temperature gradient and the SGS stress tensor. While the classical dynamic eddy thermal diffusivity SGS heat flux model requires the SGS heat flux to be aligned with the negative of the resolved temperature gradient, the three approaches proposed by Wang *et al.*¹⁵ admit more degrees of freedom. This is expected to provide more realistic geometrical and physical representations of the SGS heat flux vector. Trias *et al.*¹⁶ propose a new family of SGS heat flux models based on the symmetric positive semi-definite tensor GG^T where $G \equiv \nabla u$ and the invariants of the GG^T tensor. Dabagh *et al.*¹⁷ investigate the underlying physics of the SGS motions in flows thanks to *a priori* tests. Their case study is the turbulent Rayleigh-Bénard convection. The authors study the most used SGS heat flux models such as Peng Davidson¹¹ and Daly and Harlow¹⁸. They observe that the parameteriza-

^{a)}Electronic mail: martin.david@promes.cnrs.fr

^{b)}Electronic mail: Author to whom correspondence should be addressed: adrien.toutant@promes.cnrs.fr

^{c)}Electronic mail: francoise.bataille@promes.cnrs.fr

tions based linearly on the resolved thermal gradient are invalid and find that the tensor-diffusivity approach becomes a crucial choice for modeling the SGS heat flux, in particular, the tensorial diffusivity that includes the SGS stress tensor.

Up to now, the subgrid heat flux is often approached with constant turbulent Prandtl number models. From the observations of the modeling of the unresolved terms in the energy equation as an eddy-diffusivity heat flux (Lilly¹⁹), Wong and Lilly²⁰ compare two dynamic subgrid closure methods to compute a turbulent Rayleigh-Benard flow. In the stratification formulation the subgrid term related to velocity-temperature is computed with the temperature gradient. This method is compared to the scaling formulation, which makes use of Kolmogorov scale analysis and compute the SGS heat flux using the grid filter width and the dissipation rate. The results show that the scaling formulation permits reducing the total computer time and obtaining relatively good agreement with DNS results. Note that this new approach works with fully developed turbulence generated by shear or buoyancy. Lappa and Inam²¹ investigate LES of hybrid forced-buoyancy convection in channels with a step. They treat the cascading behavior of thermal energy in a fashion similar to that used for the turbulent kinetic energy and add a turbulent thermal diffusivity to that of the fluid as proposed by Wong and Lilly²⁰. They observe results consistent with DNS in terms of number of plumes present in the domain at a given instant and related velocity of propagation in the downstream direction. Wang and Pletcher²² perform LES of a turbulent channel flow with significant heat transfer. They use the extension of the Germano²³ subgrid model proposed by Moin²⁴. To approximate the turbulent heat flux a gradient transport model is used associated with a constant turbulent Prandtl number. Dailey *et al.*²⁵ compute two-dimensional, laminar, hydrodynamically, and thermodynamically developing channel flow with constant wall heating rates to study the quasi-developed region far downstream from the entrance region. The authors use a gradient transport formulation to approximate the turbulent heat flux. The effects of strong heating and cooling on the flow were investigated and compared with the results obtained under low heating conditions. Xie *et al.*²⁶ propose to model the SGS force and the divergence of SGS heat flux of compressible isotropic turbulence by an artificial neural network. The unclosed SGS force and divergence of SGS heat flux are approximated based on the local stencil geometry with Galilean invariance. Abkar and Moin²⁷ propose an extension of the AMD model²⁸ to compute the subfilter scalar flux. This approach is named the minimum-dissipation scalar transport model. This model is successfully assessed in thermally stratified atmospheric boundary layers. The results show that it accurately estimates the expected surface-layer similarity profiles and power spectra for both velocity and scalar concentration.

A large number of two-layer mixed models have been investigated in isothermal configurations, see Ref.^{29–32}. These works highlight the good performances of the benefits associated with the use of two-layer mixed models. Particularly, Streher *et al.*³² propose a formulation that permits to take the various flow phenomena present in near-wall turbulence into

account with the two models. Farther away from the wall, only the structural model is used because it allows capturing the interaction between turbulent structures that characterize this region. The authors obtained excellent results in isothermal channel flow at friction Reynolds number of 180, 395, and 950.

Some recent studies deal with the effect of temperature gradients in channel flow and prove the interest to investigate anisothermal channel flows. Wang *et al.*¹⁵ explore the effects of variable viscosity and thermal conductivity on the turbulent heat transport at a friction Reynolds number of 395 thanks to LES. Serra *et al.*³³ study the asymmetric reverse transition phenomenon in internal turbulent channel flows due to temperature gradients at low Reynolds number.

To the author's knowledge, there is no study dealing with the evaluation of two-layer SGS heat flux models in the operating conditions of solar receivers. Furthermore, there are very few studies that address model reliability for several thermal conditions. This paper aims to assess several T-LES approaches in extreme conditions that are characterized by a highly turbulent flow associated with strong asymmetrical heating. The influence of the mesh and the thermal conditions are also investigated to assess the reliability of the models.

The paper is organized as follows. The simplified gas-pressurized solar receiver is described in Sec. II. The resolved equations, the numerical setting, and the investigated T-LES methods are presented in Sec. III. The results of the simulations are given and discussed in Sec. IV. A final section concludes.

II. SIMPLIFIED GAS-PRESSURIZED SOLAR RECEIVER

The investigated geometry is similar to the shape of external gas-pressurized solar receivers of concentrated solar power towers. It is supposed to be an infinitely long and wide channel. One wall of the channel is directly irradiated by concentrated solar light (designated as "hot wall") whereas the other is insulated (designated as "cold wall"). In this study, T-LES are performed in a fully developed three-dimensional turbulent channel flow asymmetrically heated. The channel is presented in Fig. 1. It consists in two periodic directions (streamwise (x) and spanwise (z) directions). The wall-normal direction (y) is enclosed by two plane walls. The channel size is $4\pi\delta \times 2\delta \times 4/3\pi\delta$ where $\delta = 3\text{mm}$. In all the simulations, the hot and cold plate temperatures are respectively set to 1300 K and 900 K. In gas-pressurized solar receivers the effusivity of the walls is much bigger than the one of the heat transfer fluid. As a consequence, the air is passing through a channel at almost constant wall temperatures. The investigated wall temperatures correspond to the maximum temperature encountered in gas pressurized solar receiver. The cold wall temperature is not adiabatic since this wall temperature is higher than the temperature of the pressurized-gas. Note that in the real configuration, the cold wall is heated by conduction inside the receiver and by radiative heat transfer with the hot wall. Notice that, the results of Avellaneda *et al.*³⁴ point that there are no significant differences between the two types of

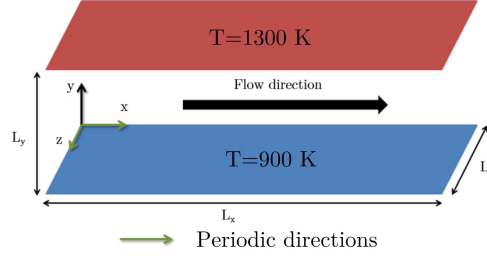


FIG. 1. Investigated channel flow.

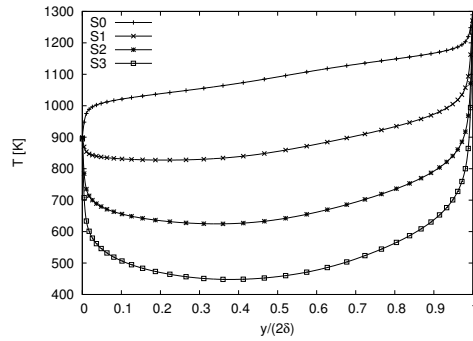


FIG. 2. Temperature profiles.

thermal boundaries conditions for turbulent low Mach channel flow under high asymmetric temperature gradient. The thermodynamical pressure, P_0 , is 10 bars. The hot wall friction Reynolds number of the simulations are lying between 621 and 648. For the cold wall, the values are lying between 968 and 1022. In all the simulations, the mean friction Reynolds number is close to 800.

A source term is added in the energy equation to obtain different temperature profiles despite the periodic boundary conditions and thus study several axial locations in the receiver. The equations are detailed in Sec. III. This source term is constant in time and homogeneous in the computational. Four temperature profiles are studied. They are displayed in Fig. 2. Each curve corresponds to a DNS performed with a fixed heat sink value. The higher the heat extraction, the lower the mean fluid temperature, traducing a location closer to the inlet of the solar receiver. The investigated thermal conditions permit testing T-LES over large fluid temperature and wall heat flux range. The simulation names are linked to heat sink values and the corresponding wall heat fluxes in Table I. Notice that, in the S0 conditions, the hot and cold wall heat fluxes are opposed: the fluid is heated from the hot wall and cooled from the cold wall. For the conditions "S1", "S2", and "S3", the fluid is heated from both walls.

TABLE I. Heat sink and wall heat fluxes associated with each simulation.

Simulation	S0	S1	S2	S3
Heat sink [MW/m^3]	0	55	109	164
Hot wall heat flux [kW/m^2]	98	263	441	587
Cold wall heat flux [kW/m^2]	-98	64	244	410

III. THERMAL LARGE EDDY SIMULATION

A. Filtered low Mach number equations

The low-Mach number Navier-Stokes equations are described in this section. This approximation aims to narrow the gap between incompressible and compressible Navier-Stokes equations and is suitable for the computation of convection in a fluid in the presence of large density gradients³⁵. The low Mach number equations consider internal wave propagation, but they do not take into account acoustic waves. Thus, the numerical methods developed for incompressible flow can be used. This approximation conducts to divide the pressure into two terms: the thermodynamical pressure which is homogeneous and the mechanical pressure. The Stokes' hypothesis is assumed³⁶. The Favre formulation is employed to filter the equations as suggested by Dupuy *et al.*³⁷. This formulation uses the density-weighted Favre filter ($\tilde{\cdot}$). The variables are defined for any field ψ as $\tilde{\psi} = \bar{\rho}\psi/\bar{\rho}$, where ($\bar{\cdot}$) is the unweighted classical filter. Nonlinear term result from the filtering of the low Mach number equations. In this study, the sub-grid terms related to the nonlinearity of momentum convection and the correlation of density and velocity are modeled as recommended by Dupuy *et al.*¹⁰. The solved equations are presented below.

- Mass conservation equation

$$\frac{\partial \tilde{\rho}}{\partial t} + \frac{\partial \tilde{\rho} \tilde{U}_j}{\partial x_j} = 0, \quad (1)$$

- Momentum conservation equation

$$\frac{\partial \tilde{\rho} \tilde{U}_i}{\partial t} = - \frac{(\partial \tilde{\rho} \tilde{U}_j \tilde{U}_i + \rho G_{U_j U_i})}{\partial x_j} - \frac{\partial P}{\partial x_i} + \frac{\partial \Sigma_{ij}(\tilde{U}, \tilde{T})}{\partial x_j}, \quad (2)$$

- Energy conservation equation

$$\frac{\partial}{\partial x_j} (\tilde{U}_j + \bar{\rho} G_{U_j / \rho}) = - \frac{1}{\gamma P_0} \left[(\gamma - 1) \left(\frac{\partial Q_j(\tilde{T})}{\partial x_j} - H_s \right) + \frac{dP_0}{dt} \right], \quad (3)$$

- Ideal gas law

$$\tilde{T} = \frac{P_0}{\bar{\rho} r} \quad (4)$$

with ρ the density, T the temperature, H_s the heat sink, γ the heat capacity ratio, $r = 287 \text{ J.kg}^{-1}.\text{K}^{-1}$ the ideal gas specific

constant, t the time, P the mechanical pressure, P_0 thermodynamical pressure, U_i the i th component of velocity, and x_i the Cartesian coordinate in the i th direction. The subgrid term relative to momentum convection is $G_{U_j U_i} = \widetilde{U_j U_i} - \widetilde{U_j} \widetilde{U_i}$ and the subgrid term relative to the density-velocity correlation is expressed as $G_{U_j/\rho} = \widetilde{U_j/\rho} - \widetilde{U_j}/\widetilde{\rho}$. The Einstein summation convention is employed. The thermodynamical pressure is obtained by integrating Eq. 3 over the volume of the studied geometry:

$$\frac{dP_0}{dt} = -(\gamma - 1) \left(\frac{1}{V} \int Q_j(\tilde{T}) dS_j - H_s \right) \quad (5)$$

with V the volume of the computational domain and S_j the boundaries of the investigated domain.

The shear-stress tensor and the conductive heat flux are respectively computed with the functions $\Sigma_{ij}(\tilde{U}, \tilde{T})$, and $Q_j(\tilde{T})$, assuming Newtonian fluid and Fourier's law, which leads to the following expressions:

$$\Sigma_{ij}(\tilde{U}, \tilde{T}) = \mu(\tilde{T}) \left(\frac{\partial \tilde{U}_i}{\partial x_j} + \frac{\partial \tilde{U}_j}{\partial x_i} \right) - \frac{2}{3} \mu(\tilde{T}) \frac{\partial \tilde{U}_k}{\partial x_k} \delta_{ij}, \quad (6)$$

$$Q_j(\tilde{T}) = -\lambda(\tilde{T}) \frac{\partial \tilde{T}}{\partial x_j}, \quad (7)$$

where $\mu(\tilde{T})$ is the dynamic viscosity, $\lambda(\tilde{T})$ is the thermal conductivity, and δ_{ij} is the Kronecker symbol.

The fluid passing through the channel is air. The Sutherland's law³⁸ is used to compute the viscosity from the temperature.

$$\mu(\tilde{T}) = \mu_0 \frac{\tilde{T}^{3/2}}{T_0} \frac{T_0 + S}{\tilde{T} + S}, \quad (8)$$

where $\mu_0 = 1.716 \times 10^{-5}$ Pa.s, $S = 110.4$ K, and $T_0 = 273.15$ K. The Prandtl number is supposed to be constant in each simulation, and the heat capacity at constant pressure C_p is obtained with the average of the wall temperatures. The conductivity is deduced from the Prandtl number, the heat capacity at constant pressure, and the viscosity.

$$\lambda(\tilde{T}) = \frac{C_p}{Pr} \mu(\tilde{T}). \quad (9)$$

Notice that the gravity term is neglected in the equations. As the distance between the hot and cold walls of the channel is small, the buoyancy force is negligible when compared to the viscous forces. The Richardson number computed at $y^+ = 30$ in the hot side of the S3 conditions, which induce the highest near wall temperature gradient, is about 0.0001. This shows that the free convection is negligible in front of the forced convection.

B. Numerical settings

The simulations are carried out using TrioCFD software³⁹. This code has been developed by the French Alternative Energies and Atomic Energy Commission and has been used

TABLE II. DNS and T-LES mesh characteristics. Dimensionless mesh size is given for the cold wall and the simulation corresponding to the highest cold friction Reynolds.

Name	Number of grid points $N_x \times N_y \times N_z$	Dimensionless mesh size $\Delta_x^+ ; \Delta_y^+(0) ; \Delta_z^+(\delta) ; \Delta_z^+$
DNS	$1152 \times 746 \times 768$	11.2 ; 0.43 ; 5.5 ; 4.3
AAA	$256 \times 152 \times 192$	50 ; 1.1 ; 33 ; 22
BAB	$192 \times 152 \times 128$	69 ; 1.1 ; 33 ; 33
CAC	$128 \times 152 \times 72$	80 ; 1.1 ; 33 ; 45

in many simulations of fluid flows^{34,37,40–45}. Computations are performed using a finite difference method in a staggered grid system. A third-order Runge-Kutta scheme is used to approach time derivatives. Momentum convection is computed using second-order or fourth-order centered schemes, depending on the simulation. Mass convection is approximated with a second-order centered second-order scheme or with a third-order QUICK scheme. Velocity divergence and temperature diffusion are discretized with centered second-order schemes.

Regarding the mesh, cells are uniform in the streamwise and spanwise directions. The cell size in the wall-normal direction follows the hyperbolic tangent law described in Eq. 10,

$$y_k = L_y \left(1 + \frac{1}{a} \tanh \left[\left(\frac{k-1}{N_y-1} \right) \tanh^{-1}(a) \right] \right) \quad (10)$$

with a the mesh dilatation parameter and N_y the number of grid points in the wall-normal direction. As the filter size of the T-LES is given by the mesh and the discretization scheme, the cell size has a significant influence on the results. For that reason, three T-LES meshes are investigated. They are given in Table II. The DNS mesh characteristics are also presented. Note that the numerical method has been validated in David *et al.*⁴⁴ by comparing an isothermal DNS at a friction Reynolds number of 930 with the reference DNS of Hoyas and Jimenez⁴⁶. For the LES meshes, the first, second, and third characters respectively correspond with the x , y , and z directions. Character "A" accounts for the highest resolution whereas "C" accounts for the coarsest resolution. The effects of the mesh resolution in the streamwise and spanwise directions are investigated. The number of grid points in the wall-normal direction is fixed to 152 for all the T-LES. The first grid point being located at $y^+ = 1$, the viscous sublayer is resolved.

C. Subgrid-scale models

The models for momentum convection and density-velocity correlation subgrid terms are expressed in Eq. 11 and 12,

$$G_{U_j U_i} \approx \tau_{ij}^{SGS}(\tilde{U}, \bar{\Delta}), \quad (11)$$

$$G_{U_j/\rho} \approx \pi_j^{SGS}(\tilde{U}, 1/\bar{\rho}, \bar{\Delta}). \quad (12)$$

The SGS terms, τ_{ij} and π_j , are computed with models that use variables resolved in T-LES. Zero algebraic models without wall function or wall model are investigated since the

first grid point is in the linear sub-layer. The investigated functional, structural, and mixed models are described in the following subsections. The filter length scale is given by $\bar{\Delta} = (\bar{\Delta}_x \bar{\Delta}_y \bar{\Delta}_z)^{1/3}$. The acronyms of the assessed models are given into brackets in the next. Note that no dynamic formulation of model is investigated since the benefit associated with dynamic procedures is not clear for the simulation of isothermal and anisothermal turbulent channel flow according to Dupuy *et al.*^{37,41} while requiring more computational time. Nonetheless, other formulations of these methods would deserve to be tested in these conditions.

1. Functional models

Functional models rely on the artificial subgrid viscosity proposed by Boussinesq⁴⁷. They assume a one-to-one correlation between the subgrid-scale stress and the large-scale deformation tensors⁴⁸. Eddy-viscosity closures assume a one-way energy transfer from the resolved to the SGS and are then often over-dissipative. The subgrid term is represented with a turbulent viscosity. The SGS tensor relative to momentum convection is computed by analogy with molecular diffusion, as expressed in Eq. 13:

$$\tau_{ij}^{SGS}(\tilde{U}, \bar{\Delta}) = -2\nu_e^{SGS}(\mathbf{g}, \mathbf{d}, \bar{\Delta})S_{ij}, \quad (13)$$

with $S_{ij} = 0.5(g_{ij} + g_{ji})$ the rate of the deformation tensor, \mathbf{g} the velocity gradient given by $g_{ij} = \partial \tilde{U}_i / \partial x_j$, and ν_e^{SGS} the turbulent viscosity which expression depends on the model used. Eddy-diffusivity models are used to approximate the density-velocity subgrid term. They involve the SGS Prandtl number, Pr_t :

$$\pi_j^{SGS}(\tilde{U}, \phi, \bar{\Delta}) = -\frac{\nu_e^{SGS}(\mathbf{g}, \mathbf{d}, \bar{\Delta})}{Pr_t} d_j, \quad (14)$$

with $d_j = \partial \phi / \partial x_j$ the scalar gradient. Pr_t is the turbulent Prandtl number. David *et al.*^{44,49} study the flow physic thanks to DNS in the four operating conditions that are investigated in this paper. They show that the turbulent Prandtl number is lying between 0.75 and 1.05 and can thus be well approximated with $Pr_t = 0.9$. No dynamic formulations of the models are investigated since Dupuy *et al.*^{37,41} state that the benefit associated with dynamic formulation is not clear for T-LES in channel flow at low Reynolds number and strong temperature gradients.

In this paper, the investigated functional closures are derived from the AMD model proposed by Rozema *et al.*²⁸. The expression of the classical AMD model given by Eq. 15:

- AMD model (denoted "AMD")

$$\nu_e^{AMD}(\mathbf{g}, \mathbf{d}, \bar{\Delta}) = C^{AMD} \frac{\max(0, -G_{ij} S_{ij}^d)}{g_{mn} g_{mn}}, \quad (15)$$

with S_{ij}^d the traceless symmetric part of the squared velocity gradient tensor and $G_{ij} = \bar{\Delta}_k^2 g_{ik} g_{jk}$ the gradient model.

The scalar AMD closure²⁷ is also used. The subgrid viscosity is then computed with the scalar gradient.

- Scalar AMD model (denoted "AMD^s")

$$\nu_e^{AMD^s}(\mathbf{g}, \mathbf{d}, \bar{\Delta}) = C^{AMD^s} \frac{\max(0, -D_j d_j)}{d_m d_m}, \quad (16)$$

where $D_j = \bar{\Delta}_k^2 g_{jk} d_k$ is the gradient model for the density-velocity correlation subgrid term. The third functional model tested is an extension of the classical AMD closure to compressible flows. This approach is described below. Eddy-viscosity closures set the sub-filter model equal to

$$\tau_{ij} - \frac{1}{3} \tau_{kk} I_{ij} = -2\nu_e \left(S_{ij} - \frac{1}{3} S_{kk} \right). \quad (17)$$

Clark *et al.*⁵⁰ show that the Taylor expansion of the sub-filter tensor gives

$$\tau_{ij} = \bar{u}_i \bar{u}_j - \bar{u}_i \tilde{u}_j = \frac{1}{12} (\Delta x_k \partial_k \tilde{u}_i) (\Delta x_k \partial_k \tilde{u}_j) + \mathcal{O}(\Delta x_i^4), \quad (18)$$

leading to the following expression of the eddy dissipation of the exact sub-filter tensor

$$-\tau_{ij} S_{ij} = -\frac{1}{12} S_{ij} (\Delta x_k \partial_k \tilde{u}_i) (\Delta x_k \partial_k \tilde{u}_j) + \mathcal{O}(\Delta x_i^4). \quad (19)$$

Using Eq. 17 and 19 and following the development proposed by Rozema *et al.*²⁸ permits obtaining the eddy viscosity expression given in Eq. 20.

- AMD model extended to compressible case (denoted "AMD^c")

$$\nu_e^{AMD^c}(\mathbf{g}, \mathbf{d}, \bar{\Delta}) = C^{AMD^c} \frac{\max(0, -(G_{ij} - \frac{1}{3} G_{kk} I_{ij}) S_{ij})}{(S_{mn} - \frac{1}{3} S_{kk} I_{mn}) S_{mn}}. \quad (20)$$

2. Structural models

Structural approaches aim to approximate the structure of the SGS stress tensor using the filtered velocity or formal series expansions. These models tend to be unstable. In this study, the Bardina⁵¹ and the scale-similarity⁵² models are assessed.

The scale similarity hypothesis relies on a double filtering approach and on the idea that the main interactions between the resolved and modeled scales involve the smallest eddies of the former and the largest eddies of the latter. It is then based upon the assumption that the statistical structure of the subgrid scales tensor is similar to that of the smallest resolved scales. According to Sagaut⁵³, this closure generally produces good results.

- Bardina model⁵¹ (denoted "Bard")

$$\tau_{ij}^{Bard} = C^{Bard} \left(\tilde{U}_i \tilde{U}_j - \tilde{\tilde{U}}_i \tilde{\tilde{U}}_j \right) \quad (21)$$

$$\pi_j^{Bard} = C^{Bard} \left(\tilde{U}_i \tilde{T} - \tilde{\tilde{U}}_i \tilde{\tilde{T}} \right) \quad (22)$$

Practically, the subgrid tensor is approximated as proposed by Streher *et al.*³², see the following equations,

– for the diagonal terms:

$$\tau_{ii} = \frac{1}{4}(U_i^n + U_i^{n+1})^2 - \frac{1}{16}(U_i^{n-1} + U_i^n + U_i^{n+1} + U_i^{n+2})^2, \quad (23)$$

– for the extra-diagonal terms:

$$\begin{aligned} \tau_{ij} = & \frac{1}{4}(U_i^{m-1} + U_i^m)(U_j^{n-1} + U_j^n) \\ & - \frac{1}{16}(U_i^{m-2} + U_i^{m-1} + U_i^m + U_i^{m+1}) \\ & (U_j^{n-2} + U_j^{n-1} + U_j^n + U_j^{n+1}), \end{aligned} \quad (24)$$

where n and m respectively represent the node number in the streamwise, respectively, spanwise direction. The SGS heat flux expression is inspired by the subgrid tensor formulation and is given by Eq. 25,

$$\pi_i = \frac{1}{2}U_i(T^{n-1} + T^n) - \frac{1}{4}U_i(T^{n-2} + T^{n-1} + T^n + T^{n+1}). \quad (25)$$

In the simulations performed with the scale similarity model, the box filter is used. It is computed as an average over three cells in the three directions.

- Scale similarity model⁵² (denoted "Sim")

$$\tau_{ij}^{sim} = C^{sim} \left(\widetilde{U_j U_i} - \widetilde{U_j} \widetilde{U_i} \right) \quad (26)$$

$$\pi_j^{sim} = C^{sim} \left(\widetilde{U_j \phi} - \widetilde{U_j} \widetilde{\phi} \right) \quad (27)$$

- Scale similarity model with variable density (denoted "Sim^c")

$$\tau_{ij}^{sim^c} = C^{sim^c} \left(\widetilde{\bar{\rho} U_j U_i} - \frac{\bar{\rho} \widetilde{U_j} \widetilde{\bar{\rho} U_i}}{\bar{\rho}} \right) \quad (28)$$

$$\pi_j^{sim^c} = C^{sim^c} \left(\widetilde{\bar{\rho} U_j \phi} - \frac{\bar{\rho} \widetilde{U_j} \widetilde{\bar{\rho} \phi}}{\bar{\rho}} \right) \quad (29)$$

3. Mixed models

Mixed approaches involve both functional and structural models to correct the drawbacks of functional and structural closures. On the one hand, the functional closures are used to provide a good approximation of the energy transfer levels between the resolved and the subgrid scales. On the other hand, the structural models permit giving an accurate estimation of the structure of the subgrid tensor and are able to capture anisotropic effects and disequilibrium^{54–56}.

In this paper, several mixed models are tested. They combine the AMD model and the Bardina model or the scale similarity model. One-layer and two-layers mixed models are investigated. One-layer mixed models are constructed with the linear combination of the two used approaches, see Eq. 30,

$$\tau_{ij} = \alpha \tau_{ij}^{func} + \beta \tau_{ij}^{struc}, \quad (30)$$

where α and β are two constants, and *func* and *struc* respectively account for the functional model and structural model. The velocity-density correlation term is obtained similarly.

The proposed two-layers mixed models are inspired by the work of Streher *et al.*³². The functional model constant decreases when the distance from the walls increases. As for the structural model, the constant is homogeneous in the computational domain. In the near wall region, this formulation permits introducing dissipation thanks to the eddy-viscosity model while accounting for the interaction between turbulent structures, as well as for backscatter of energy thanks to the structural model. In the center region of the channel, the weight associated with the functional model is reduced since the viscous stresses are less important than the turbulent stresses, which are well approximated by the structural approach. The applied function is given by Eq. 31. This method has recently been used by Streher *et al.*³² and provides very good results in isothermal channel flow.

$$C_i^{func} = C^{func} + \left(0, 5 + 0, 5 \tanh \left(\frac{y_i - s_c}{s_f} \right) \right) (C_c - C^{func}) \quad (31)$$

where i is the number of the i^{th} cell in the wall-normal direction, y is the distance from the wall, $s_f = 0.00016252$ is the smoothing factor, $s_c = 0.00023217$ is the smoothing center and C_c is the value of the constant in the center of the channel. Smoothing factor and smoothing center parameter values are those recommended by Streher *et al.*³². They aim to model the near wall region, and particularly the velocity fluctuation peaks, with the two type of closures.

4. Investigated T-LES approaches

The investigated T-LES approaches and their acronyms are described in Table III. The results of the simulations performed with only the Bardina model are not presented because the computations diverge. This study does not intend to provide an exhaustive benchmark but to assess several configurations regarding their potential of giving accurate and reliable results. The tests obtained by David *et al.*^{44,45} and Streher *et al.*³² also oriented the authors' choice.

IV. RESULTS AND DISCUSSION

The simulation results are spatially-averaged in the streamwise and spanwise directions. Once the steady state is reached, they are time-averaged. This combination of averages is denoted by $\langle \cdot \rangle$. To provide a rigorous comparison be-

TABLE III. Investigated SGS models. The superscript (\cdot^c) is employed for the models that are designed for the study of compressible flows. The acronyms "AMD^c", "Sim", and "Bard" respectively account for the following subgrid-scale models: scalar AMD, scale similarity, and Bardina. The value of the constant in the center of the channel is indicated by the value in brackets in the column "Type". Note that for the one-layer model, the constant is homogeneous in the computational domain.

Simulation name	Short name	Functional model		Structural model		Type (cc)	Numerical scheme	
		name	constant	name	constant		momentum conv.	mass conv.
nomodel (c2-c2)	N1	\emptyset	\emptyset	\emptyset	\emptyset	\emptyset	c2	c2
nomodel (c4-c2)	N2	\emptyset	\emptyset	\emptyset	\emptyset	\emptyset	c4	c2
A03-A03 (c2-c2)	F1	AMD-AMD	0.3-0.3	\emptyset	\emptyset	1L	c2	c2
A03-A03 (c4-c2)	F2	AMD-AMD	0.3-0.3	\emptyset	\emptyset	1L	c4	c2
A03-As03 (c2-c2)	F3	AMD-AMD ^c	0.3-0.3	\emptyset	\emptyset	1L	c2	c2
Ac03-Ac03 (c2-c2)	F4	AMD ^c -AMD ^c	0.3-0.3	\emptyset	\emptyset	1L	c2	c2
Ac03-Ac03 (c4-c2)	F5	AMD ^c -AMD ^c	0.3-0.3	\emptyset	\emptyset	1L	c4	c2
S1 (c4-c2)	T1	\emptyset	\emptyset	Sim- \emptyset	1- \emptyset	1L	c4	c2
Sc1 (c4-c2)	T2	\emptyset	\emptyset	Sim ^c - \emptyset	1- \emptyset	1L	c4	c2
Sc1-S1 (c4-c2)	T3	\emptyset	\emptyset	Sim ^c -Sim	1-1	1L	c4	c2
A02+B1-A02+B1 1L (c2-c2)	M1	AMD-AMD	0.2-0.2	Bard-Bard	1-1	1L	c2	c2
A05+B06-A05+B06 2L cc015 (c2-c2)	M2	AMD-AMD	0.5-0.5	Bard-Bard	0.6-0.6	2L (0.15)	c2	c2
A05+B06-A05+B06 2L cc0 (c2-c2)	M3	AMD-AMD	0.5-0.5	Bard-Bard	0.6-0.6	2L (0)	c2	c2
A06+B05-A06+B04 2L cc015 (c2-c2)	M4	AMD-AMD	0.6-0.6	Bard-Bard	0.5-0.4	2L(0.15)	c2	c2
A06+B05-A06+B04 2L cc015 (c4-c2)	M5	AMD-AMD	0.6-0.6	Bard-Bard	0.5-0.4	2L(0.15)	c4	c2
A06+Sc05-A06+S04 2L cc015 (c4-c2)	M6	AMD-AMD	0.6-0.6	Sim ^c -Sim	0.5-0.4	2L(0.15)	c4	c2

tween T-LES and DNS, the modeled terms of T-LES are systematically added to the associated quantity. This is shown, for the Reynolds stress tensor, by the following proof:

$$R_{ij}^{DNS} = \langle U_i U_j \rangle - \langle U_i \rangle \langle U_j \rangle \simeq \langle \tilde{U}_i \tilde{U}_j \rangle - \langle \tilde{U}_i \rangle \langle \tilde{U}_j \rangle, \quad (32)$$

$$R_{ij}^{DNS} = \langle \tilde{U}_i \tilde{U}_j \rangle + \langle \tilde{U}_i \tilde{U}_j - \tilde{U}_i \tilde{U}_j \rangle - \langle \tilde{U}_i \rangle \langle \tilde{U}_j \rangle, \quad (33)$$

$$R_{ij}^{DNS} = \langle \tilde{U}_i \tilde{U}_j \rangle + R_{ij}^{LES} - \langle \tilde{U}_i \rangle \langle \tilde{U}_j \rangle, \quad (34)$$

$$R_{ij}^{DNS} = R_{ij}^{LES} + \langle \tau_{ij}^{SGS} \rangle. \quad (35)$$

The reconstruction of the Reynolds stresses is commonly achieved to compare LES with DNS. The method has notably been investigated by Winckelmans *et al.*⁵⁷. The DNS deviatoric Reynolds stress tensor, $R_{ij}^{DNS,dev}$ is compared to the LES deviatoric Reynolds stress tensor, $R_{ij}^{LES,dev}$, and the averaged deviatoric SGS stress tensor, $\langle \tau_{ij}^{SGS} \rangle^{dev}$ as described in Eq. 36

$$R_{ii}^{DNS,dev} = R_{ii}^{LES,dev} + \langle \tau_{ii}^{SGS}(\tilde{\mathbf{U}}, \tilde{\Delta}) \rangle^{dev} \quad (36)$$

with $R_{ii}^{DNS} = \langle U_i U_i \rangle - \langle U_i \rangle \langle U_i \rangle$ and $R_{ii}^{LES} = \langle \tilde{U}_i \tilde{U}_i \rangle - \langle \tilde{U}_i \rangle \langle \tilde{U}_i \rangle$. Note that the coordinates x, y, z and x_1, x_2, x_3 as well as U, V, W and U_1, U_2, U_3 are used interchangeably for practical reasons.

$$R_{ij}^{DNS} = R_{ij}^{LES} + \langle \tau_{ij}^{SGS}(\tilde{\mathbf{U}}, \tilde{\Delta}) \rangle, \text{ for } i \neq j \quad (37)$$

Concerning the velocity-temperature correlations, the same procedure is applied.

$$R_{i\theta}^{DNS} = R_{i\theta}^{LES} + \langle \pi_i^{SGS}(\tilde{\mathbf{U}}, \tilde{T}, \tilde{\Delta}) \rangle \quad (38)$$

where $R_{i\theta}^{DNS} = \langle U_i \theta \rangle - \langle U_i \rangle \langle \theta \rangle$ and $R_{i\theta}^{LES} = \langle \tilde{U}_i \tilde{\theta} \rangle - \langle \tilde{U}_i \rangle \langle \tilde{\theta} \rangle$. Note that, the ideal gas law permits linking $\pi_i^{SGS}(\tilde{\mathbf{U}}, \tilde{T}, \tilde{\Delta})$ to $\pi_i^{SGS}(\tilde{\mathbf{U}}, 1/\bar{p}, \tilde{\Delta})$ with the ratio r/P_0 .

The classical scaling, denoted (\cdot^+) , is used to normalized the variables. They are defined as follows: $x_i^+ = x_i U_\tau / \nu$, $U_i^+ = U_i / U_\tau$, $\langle R_{ij} \rangle^+ = \langle R_{ij} \rangle / U_\tau^2$, and $\langle U_i' \theta' \rangle^+ = \langle U_i' \theta' \rangle / (U_\tau \theta_\tau)$. The friction velocity and the friction temperature are respectively given by $U_\tau = \sqrt{\nu \partial U / \partial x_2}$, and $\theta_\tau = \phi_w / (\rho C_p U_\tau)$, with ϕ_w the conductive wall heat flux.

In subsection IV B, the results of 16 T-LES models are presented and discussed for three meshes in the operating condition "S0". Then, three T-LES are selected for detailed analysis in subsection IV C. This last subsection is divided into two parts: (1) the effects of the mesh on the turbulence statistics are analyzed and (2) the influence of the operating conditions is discussed. Notice that, flow physic has already been discussed in Ref.^{44,49}. For that reason, in this paper, the flow physics is only discussed to highlight some T-LES behaviors.

A. Data processing

To quantify the performance of the 16 T-LES, relative errors between the T-LES and the DNS are computed for each quantity. The used algorithm is given below. Firstly, the DNS results are interpolated on the mesh used for T-LES, then the relative error of each T-LES on a given quantity is computed

as follows :

$$\begin{aligned} \varepsilon_X^{T-LES_j} = & \frac{\sum_{i=1}^{N_y/2} \log\left(\frac{y_{i+1}}{y_i}\right) \left| \left(X_i^{T-LES_j} - X_i^{DNS} \right) X_i^{T-LES_j} \right|}{\sum_{i=1}^{N_y} \log\left(\frac{y_{i+1}}{y_i}\right) X_i^{DNS^2}} \\ & + \frac{\sum_{i=1}^{N_y/2} \log\left(\frac{2\delta - y_{i+1}}{2\delta - y_i}\right) \left| \left(X_{Ny/2-i+1}^{T-LES_j} - X_{Ny/2-i+1}^{DNS} \right) X_{Ny/2-i+1}^{T-LES_j} \right|}{\sum_{i=1}^{N_y} \log\left(\frac{2\delta - y_{i+1}}{2\delta - y_i}\right) X_i^{DNS^2}} \end{aligned} \quad (39)$$

where ε is the relative error, X is the considered quantity, $T-LES_j$ denotes the j th tested model, y_i is the i^{th} point in the wall-normal direction, and δ is the half height of the channel. Note that the logarithmic ratio is used to amplify the importance of near-wall values. Furthermore, the differences computed in the absolute values are weighted by the local value to augment the importance of peak values.

Then, the final errors of the j th T-LES model on mean quantities (Err_{mean}) and covariance (Err_{rms}) are computed by adding the error obtained for each value and dividing this sum by the results of the worst model, see Eq. 40- 41,

$$Err_{mean}^{LES,j} = \frac{\sum_X \varepsilon_X^{LES_j}}{\max\left(\sum_X \varepsilon_X^{LES}\right)}, \quad (40)$$

where X is successively U , V , T and ϕ ,

$$Err_{rms}^{LES,j} = \frac{\sum_X \varepsilon_X^{LES_j}}{\max\left(\sum_X \varepsilon_X^{LES}\right)}, \quad (41)$$

where X is successively the square root of $\langle u'u' \rangle^{dev}$, $\langle v'v' \rangle^{dev}$, $\langle w'w' \rangle^{dev}$, $\langle \theta'\theta' \rangle$, $\langle u'v' \rangle$, $\langle u'\theta' \rangle$, and $\langle v'\theta' \rangle$. The global error (Err_{glob}) is also presented. It is obtained as follows:

$$Err_{glob}^{T-LES,j} = \frac{nErr_{mean}^{LES,j} + mErr_{rms}^{LES,j}}{n+m}, \quad (42)$$

where n and m are respectively the numbers of studied mean quantities and correlations.

B. Global assessment of T-LES

The T-LES models are tested on the first and second-order statistics presented in subsection IV A. The normalized errors of the T-LES are displayed in Fig. 3. The results obtained on the coarsest, average, and finest meshes are respectively presented in dark-red, orange, and yellow color. The top, middle, and bottom graphs respectively give the T-LES errors on mean quantities, correlations, and the global error. Focusing on the bottom graph and for a given mesh, the results show that the

best results are obtained with the simulations involving two-layer mixed models. The simulation denoted "M4" provides particularly good results for all the tested meshes. This T-LES is among the best for the estimation of first-order statistics and provides the closest results from the DNS for the investigated second-order statistics. The value of the AMD model of 0.15 at the center of the channel permits ensuring the convergence of the simulation and helps provide good estimations of the wall heat fluxes. Focusing on the simulations performed without a model, it appears that the results are strongly influenced by the numerical scheme used for the discretization of the momentum convection. The good results obtained with the "N2" LES on mean quantities can be explained by the fact that the second order central scheme mimics the smooth filter and thus behave like a modeled subgrid term. Globally, the nomodel simulation "N1" provides the poorest results. Regarding the functional and structural approaches, mesh refinement is valuable for all the tested models on second-order statistics and global error. Compared to the T-LES carried out with the second-order scheme to approximate the momentum convection, the results are improved when the fourth-order scheme is used. Among the functional closures, both the "F2" and the "F5" T-LES produce relatively good results. As for the structural models, the "T2" T-LES produces significantly better results than the "T1" simulation (scale-similarity for incompressible cases) on the first-order statistics for all the tested meshes. The second-order statistics are also improved. Results not detailed in this paper show that the compressible formulation of the scale-similarity permits significantly enhancing the model accuracy on the wall heat fluxes (from 15% error to 0.2% error with the CAC mesh and from 11% error to 1.4% error with the AAA mesh). The "T3" simulation is in poor agreement with the DNS, particularly with the CAC and BAB meshes.

The "N2", "F5", and "M4" simulations are selected for detailed analyzes of the mesh effects (Sec. IV C 1) and the influence of the thermal conditions (Sec. IV C 2) on the model performance. Note that the acronym associated with the "M4" simulation ("A06+B05-A06+B04 2L cc015 (c4-c2)") is simplified in "mixed" in the following figures of this paper for practical reasons.

C. Detailed results of the selected models

1. Effects of the mesh

Results obtained with the selected simulations are detailed here. They are divided into two parts. Firstly, mean quantities are presented then covariances and rms values are studied.

a. First-order statistics The results associated with the first-order statistics are discussed in this paragraph. Fig. 4 displays the relative error of the three selected closure method for the three meshes on the mean quantities. The y-axis is presented with a logarithmic scale. The results show that the temperature profile is very well estimated by the three T-LES with an error inferior to 1%. The nomodel simulation gives a very good approximation of all the mean quantities. Indeed,

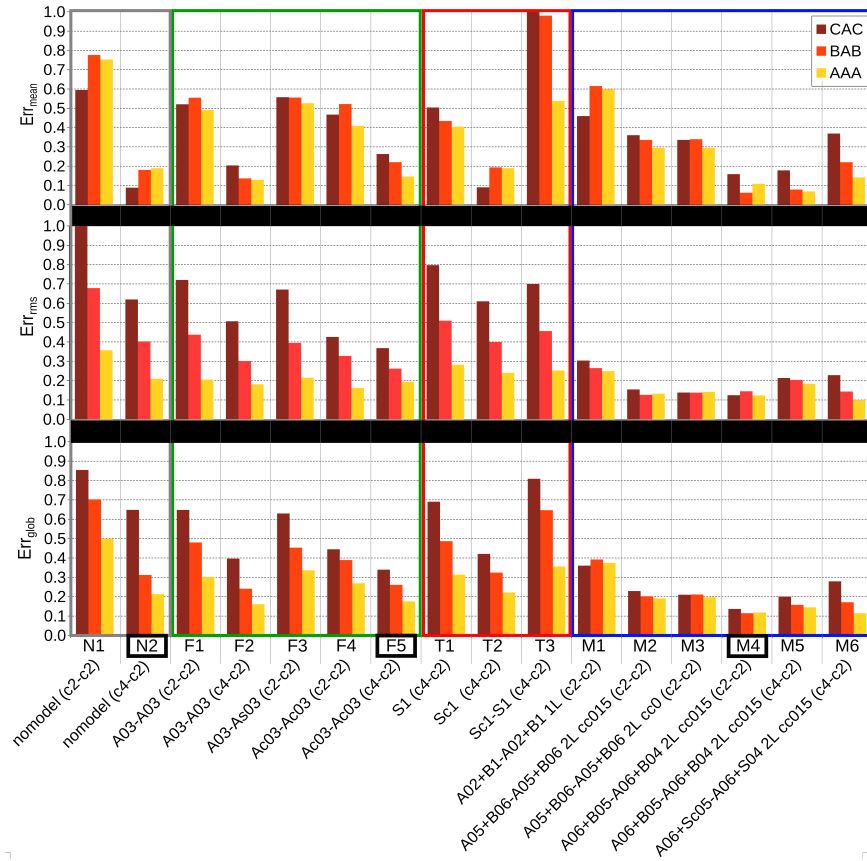


FIG. 3. Normalized error of 16 T-LES for three meshes. From top to bottom, the error is related to mean quantities, correlations, and global error. Dark-red, orange, and yellow colors respectively stand for the coarsest, average, and finest mesh. The histograms are divided into four parts that are associated with a model type. The grey, green, red, and blue boxes respectively indicate nomodel, functional models, structural models, and mixed models T-LES. The short name of the simulations is given at the bottom. The short names of the selected simulations are enclosed in black boxes.

the maximum error is committed on the streamwise velocity and it is below 3%. The error associated with the functional model on the streamwise velocity is divided by two when the mesh is refined from CAC to AAA computational setup. The wall heat flux is estimated within 2% error for all the tested meshes. The error collapses to 0.2% with the AAA mesh. The functional and mixed models give similar results for the wall-normal velocity. The two-layer approach permits estimating the streamwise velocity and the wall heat flux with an error inferior to 1.2% with the two finest meshes. The results obtained with the CAC computational setup have a margin of error of 4% at most on the mean quantities.

The classically normalized longitudinal velocity, wall-

normal velocity, and temperature profiles are plotted as functions of the wall-normal direction in Fig. 5. Regarding the streamwise velocity, all the T-LES are in very good agreement with the DNS from the wall to $y^+ = 10$, *i.e.* the beginning of the buffer layer. The nomodel simulation tends to underestimate the velocity profile at both walls. The results are deteriorated when the mesh is refined which is explained by the numerical error compensation occurring with the CAC mesh. On the contrary, the *AMD^c* approach overestimates the profile. This was also observed with the classical *AMD* model in isothermal configuration and at a friction Reynolds number of 590 by Streher *et al.*³² and in anisothermal condition at mean friction Reynolds numbers of 180 and 395 by Dupuy *et*

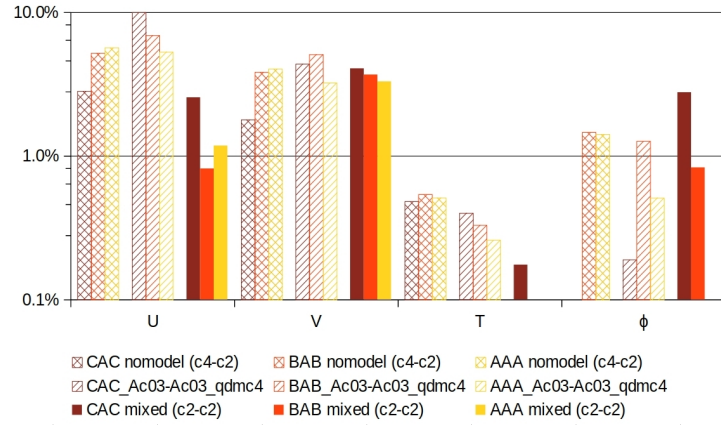


FIG. 4. Relative error on first-order statistics for the three selected T-LES approaches on the three meshes. Dark-red, orange, and yellow colors respectively stand for the coarsest, average, and finest mesh. When no bar is observed, it means that the error is inferior to 0.1%.

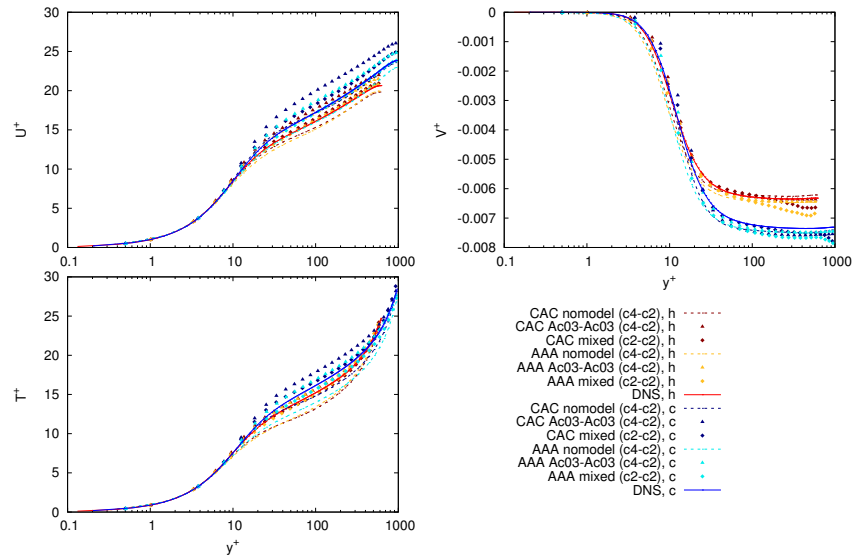


FIG. 5. Profiles of classically normalized streamwise velocity, wall-normal velocity and temperature as functions of the wall-normal direction.

*al.*³⁷. The estimation is improved with the finest mesh. As for the mixed model, it is in good agreement with the DNS profile with the CAC mesh and gives an excellent estimation when used with the AAA mesh. Note that, the influence of the mesh is bigger in the cold side than in the hot side because the

dimensionless cell size is smaller near the hot wall due to the increase in the fluid viscosity. Focusing on the wall-normal profile, it appears that all the T-LES give good approximations of the DNS results. This may due to the fact that this quantity is involved in the balance of the energy equation.

The mixed model does not reproduce the plateau, observed for normalized wall-normal distance superior to $y^+ = 70$. The functional closure is in very good agreement with the DNS. The results on the wall-normal velocity are poorly influenced by the refinement of the mesh in the streamwise and spanwise directions. As for the temperature profile, the same observations can be made as for the streamwise velocity profile. The very good agreement of the mixed model with the DNS can be highlighted.

b. Second-order statistics Second-order statistics are more difficult to predict than the mean quantities. They constitute a great challenge for LES.

Fig. 6 exposes the relative error of the three selected models for the three meshes on the correlations. The velocity cross-correlation is usually well estimated with LES in isothermal conditions^{32,41,58,59}. It seems to be also observed in strongly anisothermal conditions since the three assessed T-LES are in good agreement with the DNS on this quantity. This is probably because the cross-correlation term is involved in the balance of the momentum equation. The nomodel simulation gives very poor estimations of the Reynolds stress tensor diagonal terms, the temperature auto-correlation, and the streamwise velocity auto-correlation when used with the CAC and BAB meshes. This is also observed in isothermal configuration, see Meyer and Sagaut⁶⁰. For the nomodel and the functional model simulations, the results are globally improved when the mesh is refined. The "AMD" approach coupled with the AAA mesh is in quite good agreement with the DNS with a maximal error of 17% on the correlations involving the velocity. As for the mixed model, it permits significantly improving the estimation of the velocity covariances thanks to the combination of the complementary behavior of the AMD (slightly over dissipative) and Bardina (under-dissipative) models. Notice that, the mixed model associated with the coarsest mesh gives all the correlations involving velocity with a margin of error of 8%. The temperature fluctuations are the most difficult to predict: none of the assessed T-LES produce satisfactory results on this quantity. These observations are in agreement with those of Dupuy *et al.*³⁷.

The profiles of the Reynolds stress tensor diagonal terms and the cross-correlation are presented in Fig. 7. The correlation peak observed around $y^+ = 13$ in DNS is reproduced by all the T-LES. However, it is overestimated, respectively considerably overestimated, by the AMD model simulation, respectively the nomodel simulation (also observed by Dupuy *et al.*^{37,41} at low friction Reynolds number). The mixed model provides a very good estimation of the hot side fluctuations with the CAC mesh and a good estimation of the cold side. For all the simulations, the peaks of the correlations are mitigated when the mesh is refined (also noticed by Rezaeiravesh and Liefvendahl⁶¹), which leads to a deterioration of the results in the case of the mixed model simulation. Notice that the quasi-plateau observed in the DNS simulation around $y^+ = 100$ and caused by the high Reynolds number effects^{46,62,63} is only reproduced by the simulation carried out with the mixed model and the AAA mesh. As for the cross-correlation, all the T-LES are in good agreement with the DNS for the peak estimation. In the logarithmic region, the "AMD" and mixed model sim-

ulations tend to underestimate the hot and cold profiles.

The correlations involving the temperature are given in Fig. 8. The $\langle u'\theta' \rangle^+$ correlation exhibits similar behavior as the diagonal terms of the Reynolds stress tensor. The nomodel simulation and the functional closure simulation tend to overestimate the fluctuation peak. The mixed model T-LES provides a quite satisfying approximation of the profile even if it is slightly underestimating the peak with the AAA mesh. The correlations between the wall-normal velocity and the temperature obtained with the T-LES are in good agreement with the DNS correlation. Nevertheless, the mixed model tends to overestimate the profile in the center area of the channel when performed with the AAA mesh. This is linked with the overestimation of the wall-normal velocity observed in Fig. 5. The temperature auto-correlation profile shows near wall peaks around $y^+ = 15$ and a central peak in the channel center. For the near-wall peaks, the same observation is made as for the velocity fluctuation peaks. Regarding the central peak, it is overestimated by the nomodel simulation and the mixed model associated with the coarsest mesh. However, when the AAA mesh is used, the mixed model produces the best results. This is in agreement with the criticisms on the eddy diffusivity assumption and show the superiority of the mixed subgrid heat flux formulation compared to the classical eddy diffusivity assumption.

2. Effects of thermal conditions

In this part, the effects of thermal conditions on the T-LES accuracy are investigated. The three selected simulations are assessed in the four operating conditions that are described in Sec. II. The mesh used for the T-LES is the coarsest one (CAC). Firstly, the first-order statistics results are discussed then the second-order results are analyzed. In the next, the studied nomodel simulation has been performed with the Quick scheme for the mass convection because the simulations in the "S2" and "S3" thermal conditions diverge when the second-order scheme is used. The Quick scheme is upwind and is thus dissipative, which permits reducing the divergence risks of the simulations.

a. First-order statistics Fig. 9 displays the relative error of the three selected models for the four thermal operating conditions on the mean quantities. Due to the heat sink, the heat flux is not the same at both walls of the channel. For that reason, the results on hot and cold wall heat fluxes are presented. The figure shows that the model accuracy on the first-order statistic does not evolve in the same way for each mean quantity. Indeed, it seems that, for the simulation performed with a heat sink, all the models provide a better estimation of the streamwise and wall-normal velocities when the average wall heat flux is lower. The temperature estimation is deteriorated when the wall heat flux increases for all the tested conditions. Regarding the cold wall heat flux, the results show that the closer the fluid temperature from the cold wall, the bigger the T-LES estimation error. This is in agreement with the analysis carried out in Ref.⁶⁴. As for the hot wall heat flux, no evident conclusion can be drawn. None of the tested clo-

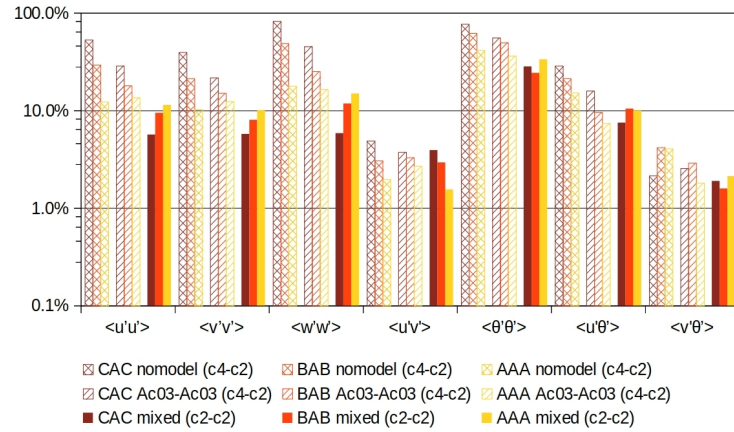


FIG. 6. Relative error on second-order statistics for the three selected T-LES approaches on the three meshes. Dark-red, orange, and yellow colors respectively stand for the coarsest, average, and finest mesh.

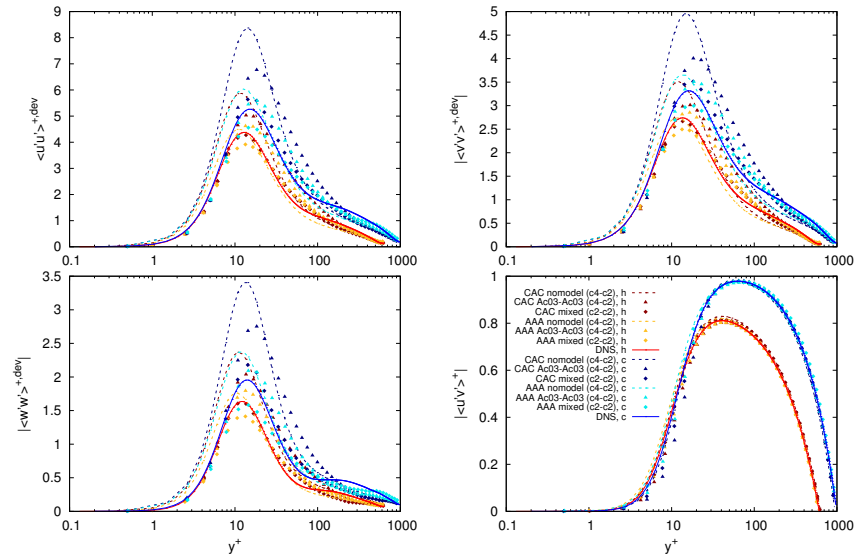


FIG. 7. Profiles of classically normalized correlations of longitudinal velocity, wall-normal velocity, transversal velocity as well as longitudinal and wall-normal velocities along the wall-normal direction of the channel.

sure produce an error inferior to 10% for all the investigated quantities. The classically normalized longitudinal velocity, wall-normal velocity, and temperature profiles are presented in Fig. 10. The streamwise velocity is quite well approxi-

mated by the nomodel simulation. The functional model produces poor results on the cold side and average results on the hot side of both thermal conditions. The streamwise velocity is underestimated by the mixed model simulation in the

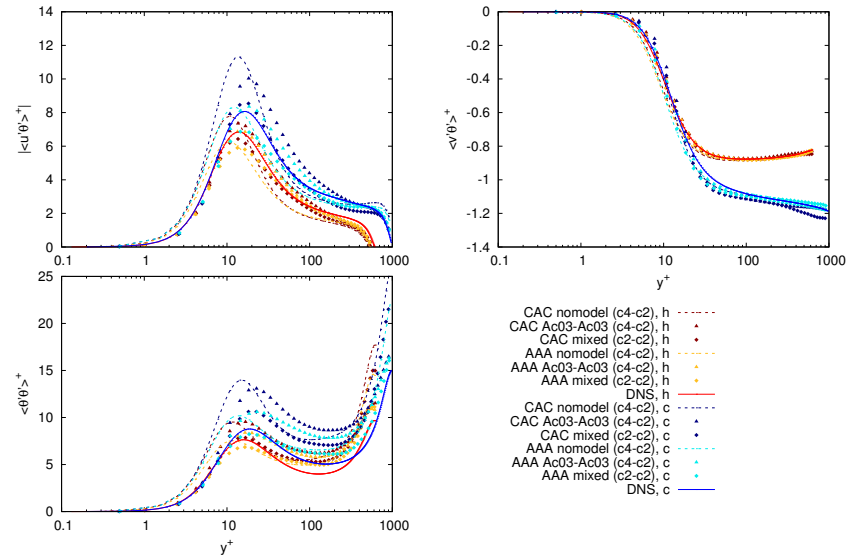


FIG. 8. Profiles of dimensionless correlations of longitudinal velocity and temperature, wall-normal velocity and temperature as well as the covariance of temperature along the wall-normal direction of the channel.

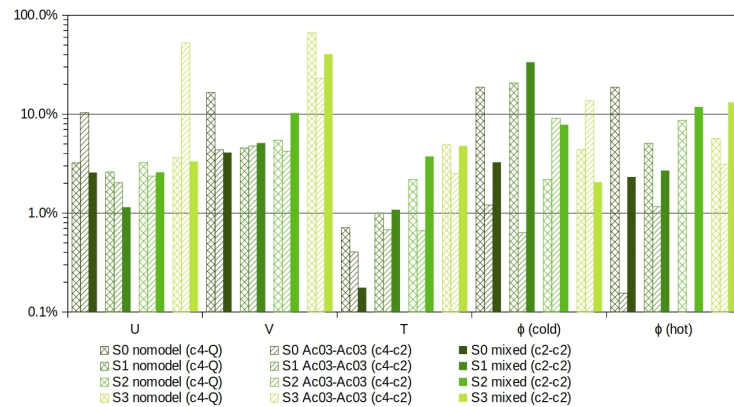


FIG. 9. Relative error on first-order statistics for the three selected T-LES approaches and the four investigated thermal conditions. The lighter the green color, the bigger the heat sink.

"S3" thermal conditions and overestimated in the "S1" thermal conditions. The wall-normal velocity is well approximated by all the T-LES in the "S1" conditions. In the "S3" conditions, the wall-normal velocity is underestimated by the "Ac03-Ac03" simulation on both sides and overestimated by the mixed model and the nomodel simulations. Regarding the

temperature profile, the functional model produces quite good results on the temperature distribution in the "S3" conditions and in the hot side of the "S1" conditions. In the cold side of the "S1" conditions, the temperature profile is overestimated for a normalized wall distance superior to $y^+ = 20$. The mixed model tends to overestimate the temperature profile for the

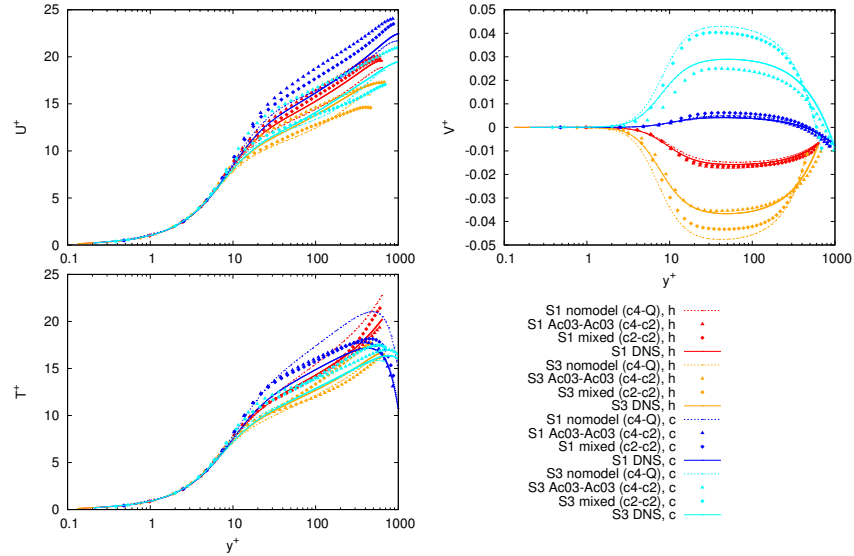


FIG. 10. Profiles of classically normalized streamwise velocity, wall-normal velocity and temperature as functions of the wall-normal direction for the thermal conditions denoted "S1" and "S3".

two presented conditions.

b. Second-order statistics Fig. 11 gives the relative error of the three selected models for the four thermal operating conditions on the correlations. The second-order statistics are a challenge for LES computations, especially in complex flows. The T-LES results might be explained by the wall-normal velocity (poorly approximated by the T-LES) that modify the turbulent structure displacements and thus affect the model accuracy on the second-order statistics. No clear tendency appears when observing the behavior of the error as a function of the thermal conditions. The nomodel simulation provides very poor quality results of the velocity fluctuations. The functional closure has a margin of error lying between 10% and 50% for "S0", "S1", and "S2" operating conditions. The error is superior to 100% in the "S3" conditions. The mixed model produces the best results among the tested LES approaches. Notice that the results are deteriorated when the heat sink increases. This is probably due to the increase of the coupling between the dynamic and the temperature which is poorly considered by the TLES. The constant turbulent Prandtl number hypothesis may not be valid in case of strong heating and/or asymmetric heating. The sub-grid term involving the temperature gradient and the thermal conductivity is neglected in this study but additional investigations are needed to assess the impact of this approximation. The $\langle u'v' \rangle$ correlation is quite well approximated by all the simulations when there is no heat sink. In the "S3" condition, which is associated with the highest heat fluxes, the er-

ror is superior to 20% for all the simulations. The estimation of the correlation of wall-normal velocity and temperature is also deteriorated when the heat flux is high. The $\langle u'\theta' \rangle$ quantity is estimated with a margin of error lying between 5% and 20%. Regarding the temperature fluctuations, the nomodel and the mixed model simulations produce similar results. The results of the functional model are significantly deteriorated when compared to the other simulations, except in the "S3" conditions. Globally, the proposed mixed model permits improving results on the second-order statistics, even if there is still room for improvement.

The profiles of the Reynolds stress tensor diagonal terms and the cross velocity correlation are presented in Fig. 12. The nomodel simulation significantly overestimates the peak of $\langle u'u' \rangle$, $\langle v'v' \rangle$, and $\langle w'w' \rangle$ fluctuations, as seen in the "S0" thermal conditions. The functional approach produces better results but the peaks are still overestimated. The mixed model gives a very good approximation in the "S3" conditions and in the hot side of the "S1" conditions and a good approximation in the cold side in the low heat flux configuration. The $\langle u'v' \rangle$ correlation is well approximated in the "S1" conditions by the two simulations carried out with models. The nomodel simulation overestimates the peak on the hot sides of both conditions. In the cold side of the "S3" configuration, the nomodel gives a good approximation of the peak by the decrease of the curve is too abrupt when compared to the DNS results. The mixed model is accurate on the hot side but significantly underestimates the cold side profile.

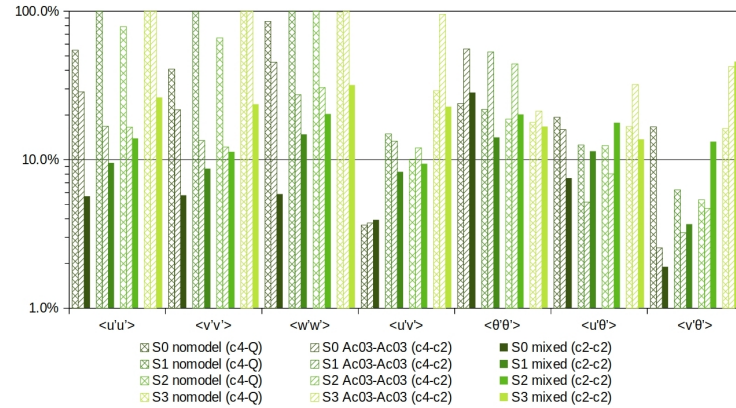


FIG. 11. Relative error on second-order statistics for the three selected T-LES approaches and the four investigated thermal conditions. The lighter the green color, the bigger the heat sink. This maximum plotted error is 100%.

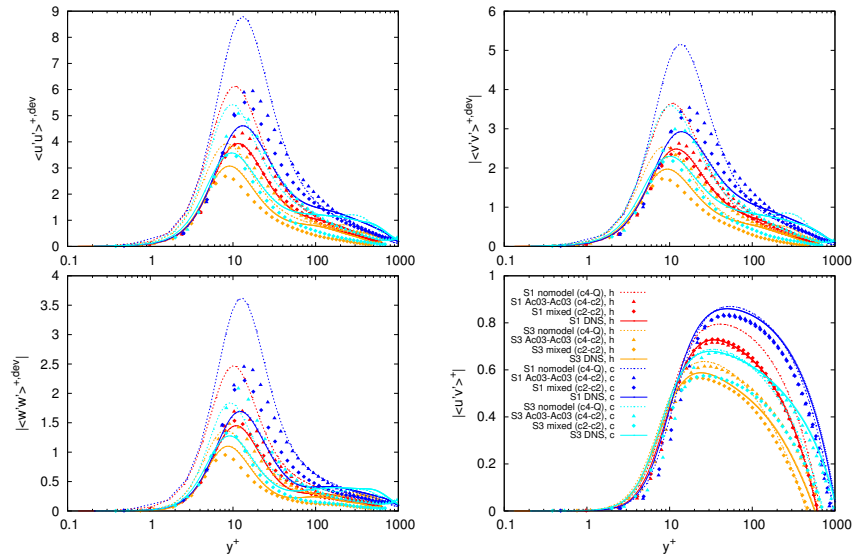


FIG. 12. Profiles of classically normalized correlations of longitudinal velocity, wall-normal velocity, transversal velocity as well as longitudinal and wall-normal velocities along the wall-normal direction of the channel for the thermal conditions denoted "S1" and "S3".

The correlations involving the temperature are presented in Fig. 13. The streamwise velocity-temperature and temperature-temperature correlations are fairly estimated by the T-LES in the "S1" conditions. Indeed, the tendencies of these profiles are reproduced. In the "S3" conditions, the T-LES give a poor approximation of the profiles. The peaks

are either significantly overestimated or significantly underestimated and, for the $\langle u'\theta' \rangle$ correlation, the tendencies of the hot and cold side profiles are not reproduced by the simulations. This means that the temperature transport is poorly estimated. Similar observations can be made for the wall-normal temperature correlation: in the "S1" conditions the profiles are

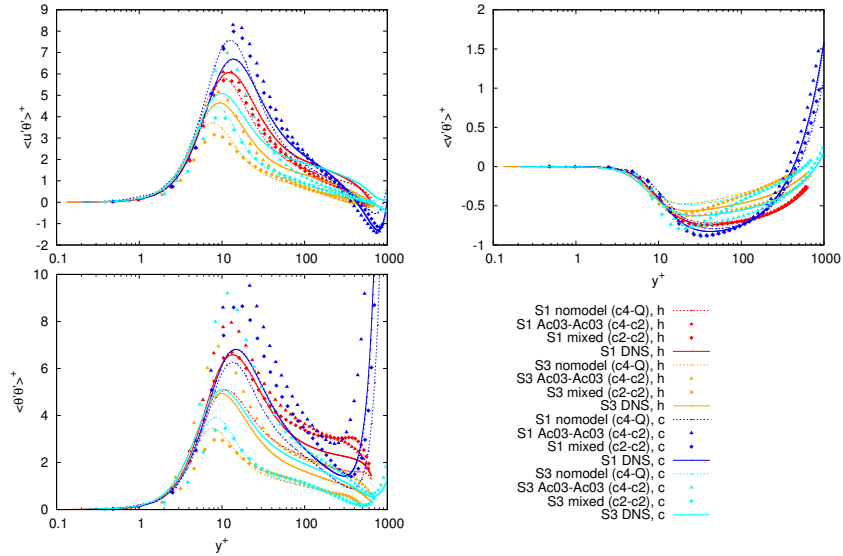


FIG. 13. Profiles of dimensionless correlations of longitudinal velocity and temperature, wall-normal velocity and temperature as well as the covariance of temperature along the wall-normal direction of the channel for the thermal conditions denoted "S1" and "S3".

well approximated but in the "S3" conditions the T-LES results are poorer. The nomodel simulation underestimates the profile amplitude, the functional model simulation overestimates it, and the mixed model does not reproduce the profile tendency.

c. *Spectral analysis* In this paragraph, 1D spectra of turbulent kinetic energy in the streamwise direction are investigated at a normalized distance of $y^+ = 40$. They are given by:

$$\int_0^{+\infty} E(k_x) dk_x = \frac{1}{2} (u_{rms}^2 + v_{rms}^2 + w_{rms}^2), \quad (43)$$

where E is the energy level and k_x is the wave number in the streamwise direction. In Figure 14, the turbulent kinetic energy spectra of T-LES are presented and compared to the DNS ones in the S0, S1, and S3 conditions. The results show that the energy content at very low wavenumber is not well captured, suggesting a difference in the production of energy at the integral scale. The T-LES tend to slightly overestimate the $-5/3$ slope in the inertial range for the three conditions. A small energy accumulation is observed in the range of the smallest resolved scale and is due to the under-resolution of these scales. This is commonly observed in LES^{65,66}. The energy levels provided by the nomodel simulations are overestimated in the S3 conditions, which are the most challenging due to the strong temperature gradients. The proposed mixed model produce a good estimation of the turbulence scales that are associated with the highest energy levels in the three in-

vestigated conditions. This can be explained by the complementary behaviors of the structural and functional models discussed in section III C.

V. CONCLUSION

In this paper, T-LES have been proposed and compared to DNS results in highly anisothermal and turbulent channel flows with the aim of improving the results of Large Eddy Simulation in the operating conditions of solar receivers. Both the velocity-velocity and the velocity-temperature correlation terms were modeled. Functional, structural, and mixed models were investigated. Firstly, a global assessment of 16 T-LES approaches have been performed. Then, three of them have been selected for more detailed investigations (1) on the mesh effect and (2) on the influence of the thermal conditions on the model accuracy.

This study shows that the T-LES results are significantly affected by the mesh resolution and the numerical scheme used for the discretization of the momentum convection term. Several numerical setups are proposed to take advantage of the numerical effects and the model behaviors. In the investigated range of grid points, refining the mesh does not necessarily lead to a better approximation of the first-order statistics. The results on second-order statistics of the investigated functional approach and the nomodel simulation are improved when the number of grid points is increased. Particularly, it permits

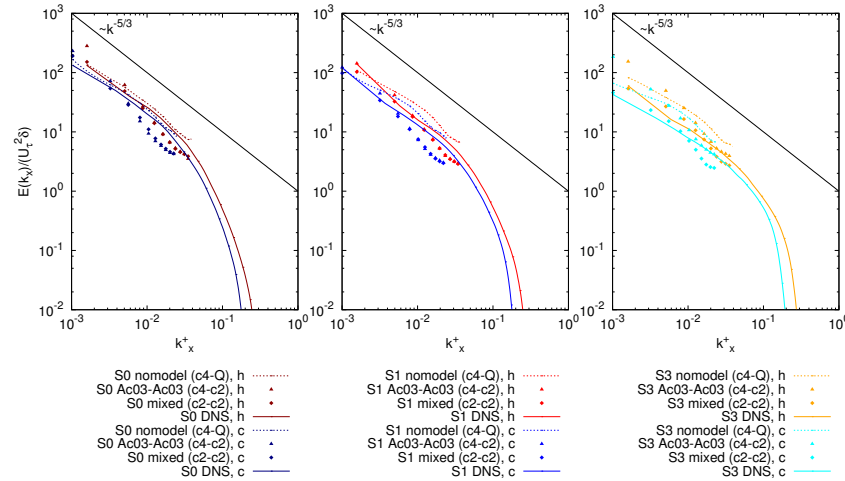


FIG. 14. One dimensional turbulent kinetic energy spectra at $y^+ = 40$ for the S0, S1, and S3 conditions.

to provide a better estimation of the correlations peaks. The mesh resolution has little influence on the wall-normal velocity, the cross-correlation, and the wall-normal and temperature correlation. The best results are obtained with the selected mixed model, which conducts to estimate the first-order statistics within 8% of error and second-order statistics within 11% of error (except the temperature fluctuations) with the three tested meshes.

Regarding the effects of thermal conditions, this study highlights the fact that the intensity of the wall heat flux has a great impact on the accuracy of the models. The T-LES best results are obtained when the bulk temperature is close to the average of the wall temperatures (*i.e.* same heat fluxes at both walls). Generally, the results are deteriorated in the conditions that are characterized by the highest heat fluxes. The strong coupling between the dynamic and the temperature is not well reproduced by the T-LES. None of the investigated models produces totally accurate results on all the tested quantities.

In the future, the influence of the subgrid terms will be investigated in those very challenging configurations and models involving artificial neural networks will be assessed with the aim of providing reliable results in different thermal operating conditions that are representative of solar receivers.

ACKNOWLEDGMENTS

The authors gratefully acknowledge the CEA for the development of the TRUST platform. This work was granted access to the HPC resources of CINES under the allocation 2022-A0112A05099 made by GENCI.

DATA AVAILABILITY STATEMENTS

The data that support the findings of this study are available from the corresponding author upon reasonable request.

- ¹M. Sedighi, R. V. Padilla, R. A. Taylor, M. Lake, I. Izadgoshasb, and A. Rose, "High-temperature, point-focus, pressurised gas-phase solar receivers: A comprehensive review," *Energy Conversion and Management* **185**, 678–717 (2019).
- ²Y. Zhou, "Turbulence theories and statistical closure approaches," *Physics Reports Turbulence Theories and Statistical Closure Approaches*, **935**, 1–117 (2021).
- ³G. Flamant, *Concentrating Solar Thermal Energy: Fundamentals and Applications* (John Wiley & Sons, 2022).
- ⁴H. J. Kull, "Theory of the Rayleigh-Taylor instability," *Physics Reports* **206**, 197–325 (1991).
- ⁵Y. Zhou, "Rayleigh–Taylor and Richtmyer–Meshkov instability induced flow, turbulence, and mixing. I," *Physics Reports Rayleigh–Taylor and Richtmyer–Meshkov Instability Induced Flow, Turbulence, and Mixing. I*, **720–722**, 1–136.
- ⁶Y. Zhou, "Rayleigh–Taylor and Richtmyer–Meshkov instability induced flow, turbulence, and mixing. II," *Physics Reports Rayleigh–Taylor and Richtmyer–Meshkov Instability Induced Flow, Turbulence, and Mixing. II*, **723–725**, 1–160 (2017).
- ⁷Y. Zhou, T. T. Clark, D. S. Clark, S. Gail Glendinning, M. Aaron Skinner, C. M. Huntington, O. A. Hurricane, A. M. Dimits, and B. A. Remington, "Turbulent mixing and transition criteria of flows induced by hydrodynamic instabilities," *Physics of Plasmas* **26**, 080901 (2019).
- ⁸Y. Zhou, R. J. R. Williams, P. Ramaprabhu, M. Groom, B. Thornber, A. Hillier, W. Mostert, B. Rollin, S. Balachandrar, P. D. Powell, A. Mahalov, and N. Attal, "Rayleigh–Taylor and Richtmyer–Meshkov instabilities: A journey through scales," *Physica D: Nonlinear Phenomena* **423**, 132838 (2021).
- ⁹A. Pouquet, D. Rosenberg, and R. Marino, "Linking dissipation, anisotropy, and intermittency in rotating stratified turbulence at the threshold of linear shear instabilities," *Physics of Fluids* **31**, 105116 (2019).

- ¹⁰D. Dupuy, A. Toutant, and F. Bataille, "A priori tests of subgrid-scale models in an anisothermal turbulent channel flow at low mach number," *International Journal of Thermal Sciences* **145**, 105999 (2019).
- ¹¹S.-H. Peng and L. Davidson, "On a subgrid-scale heat flux model for large eddy simulation of turbulent thermal flow," *International Journal of Heat and Mass Transfer* **45**, 1393–1405 (2002).
- ¹²C. W. Higgins, M. B. Parlange, and C. Meneveau, "The heat flux and the temperature gradient in the lower atmosphere," *Geophysical Research Letters* **31** (2004).
- ¹³A. Leonard, "Large-eddy simulation of chaotic convection and beyond," in *35th Aerospace Sciences Meeting and Exhibit*, Aerospace Sciences Meetings (American Institute of Aeronautics and Astronautics, 1997).
- ¹⁴J. Smagorinsky, "General circulation experiments with the primitive equations," *Monthly Weather Review* **91**, 99–164 (1963).
- ¹⁵B.-C. Wang, E. Yee, D. J. Bergstrom, and O. Iida, "New dynamic subgrid-scale heat flux models for large-eddy simulation of thermal convection based on the general gradient diffusion hypothesis," *Journal of Fluid Mechanics* **604**, 125–163 (2008).
- ¹⁶F. X. Trias, D. Folch, A. Gorobets, and A. Oliva, "Building proper invariants for eddy-viscosity subgrid-scale models," *Physics of Fluids* **27**, 065103 (2015).
- ¹⁷F. Dabbagh, F. X. Trias, A. Gorobets, and A. Oliva, "A priori study of subgrid-scale features in turbulent Rayleigh-Bénard convection," *Physics of Fluids* **29**, 105103 (2017).
- ¹⁸B. J. Daly and F. H. Harlow, "Transport Equations in Turbulence," *The Physics of Fluids* **13**, 2634–2649 (1970).
- ¹⁹D. K. Lilly, "On the numerical simulation of buoyant convection," *Tellus* **14**, 148–172 (1962).
- ²⁰V. C. Wong and D. K. Lilly, "A comparison of two dynamic subgrid closure methods for turbulent thermal convection," *Physics of Fluids* **6**, 1016–1023 (1994).
- ²¹M. Lappa and S. Inam, "Large eddy simulation of three-dimensional hybrid forced-buoyancy convection in channels with a step," *International Journal of Heat and Mass Transfer* **202**, 123767 (2023).
- ²²W.-P. Wang and R. H. Pletcher, "On the large eddy simulation of a turbulent channel flow with significant heat transfer," *Physics of Fluids* **8**, 3354–3366 (1996).
- ²³M. Germano, U. Piomelli, P. Moin, and W. H. Cabot, "A dynamic subgrid-scale eddy viscosity model," *Physics of Fluids A: Fluid Dynamics* **3**, 1760–1765 (1991).
- ²⁴P. Moin, K. Squires, W. Cabot, and S. Lee, "A dynamic subgrid-scale model for compressible turbulence and scalar transport," *Physics of Fluids A: Fluid Dynamics* **3**, 2746–2757 (1991).
- ²⁵L. D. Bailey, N. Meng, and R. H. Pletcher, "Large Eddy Simulation of Constant Heat Flux Turbulent Channel Flow With Property Variations: Quasi-Developed Model and Mean Flow Results," *Journal of Heat Transfer* **125**, 27–38 (2003).
- ²⁶C. Xie, K. Li, C. Ma, and J. Wang, "Modeling subgrid-scale force and divergence of heat flux of compressible isotropic turbulence by artificial neural network," *Physical Review Fluids* **4**, 104605 (2019).
- ²⁷M. Abkar, H. J. Bae, and P. Moin, "Minimum-dissipation scalar transport model for large-eddy simulation of turbulent flows," *Physical Review Fluids* **1**, 041701 (2016).
- ²⁸W. Rozema, H. J. Bae, P. Moin, and R. Verstappen, "Minimum-dissipation models for large-eddy simulation," *Physics of Fluids* **27**, 085107 (2015).
- ²⁹B. Vreman, B. Geurts, and H. Kuerten, "On the formulation of the dynamic mixed subgrid-scale model," *Physics of Fluids* **6**, 4057–4059 (1994).
- ³⁰K. Horiuti, "A new dynamic two-parameter mixed model for large-eddy simulation," *Physics of Fluids* **9**, 3443–3464 (1997).
- ³¹G. S. Winckelmans, A. A. Wray, O. V. Vasilyev, and H. Jeanmart, "Explicit-filtering large-eddy simulation using the tensor-diffusivity model supplemented by a dynamic Smagorinsky term," *Physics of Fluids* **13**, 1385–1403 (2001).
- ³²L. B. Streher, M. H. Silvis, P. Cifani, and R. W. C. P. Verstappen, "Mixed modeling for large-eddy simulation: The single-layer and two-layer minimum-dissipation-Bardina models," *AIP Advances* **11**, 015002 (2021).
- ³³S. Serra, E. Franquet, V. Boutrouche, and R. Manceau, "Asymmetric reverse transition phenomenon in internal turbulent channel flows due to temperature gradients," *International Journal of Thermal Sciences* **159**, 106463 (2021).
- ³⁴J. M. Avellaneda, F. Bataille, and A. Toutant, "DNS of turbulent low Mach channel flow under asymmetric high temperature gradient: Effect of thermal boundary condition on turbulence statistics," *International Journal of Heat and Fluid Flow* **77**, 40–47 (2019).
- ³⁵S. Paolucci, "Filtering of sound from the Navier-Stokes equations," NASA STI/Recon Technical Report N **83** (1982).
- ³⁶M. V. Papalexandris, "On the applicability of Stokes' hypothesis to low-Mach-number flows," *Continuum Mechanics and Thermodynamics* **32**, 1245–1249 (2020).
- ³⁷D. Dupuy, A. Toutant, and F. Bataille, "A posteriori tests of subgrid-scale models in strongly anisothermal turbulent flows," *Physics of Fluids* **31**, 065113 (2019).
- ³⁸W. Sutherland, "The viscosity of gases and molecular force," *The London, Edinburgh, and Dublin Philosophical Magazine and Journal of Science* **36**, 507–531 (1893).
- ³⁹C. Calvin, O. Cueto, and P. Emonot, "An object-oriented approach to the design of fluid mechanics software," *ESAIM: Mathematical Modelling and Numerical Analysis - Modélisation Mathématique et Analyse Numérique* **36**, 907–921 (2002).
- ⁴⁰A. Toutant, "Numerical simulations of unsteady viscous incompressible flows using general pressure equation," *Journal of Computational Physics* **374**, 822–842 (2018).
- ⁴¹D. Dupuy, A. Toutant, and F. Bataille, "A posteriori tests of subgrid-scale models in an isothermal turbulent channel flow," *Physics of Fluids* **31**, 045105 (2019).
- ⁴²F. Aulery, D. Dupuy, A. Toutant, F. Bataille, and Y. Zhou, "Spectral analysis of turbulence in anisothermal channel flows," *Computers & Fluids A Special Issue in Honor of Cecil "Chuck" E. Leith*, **151**, 115–131 (2017).
- ⁴³M. David, A. Toutant, and F. Bataille, "Numerical development of heat transfer correlation in asymmetrically heated turbulent channel flow," *International Journal of Heat and Mass Transfer* **164**, 120599 (2021).
- ⁴⁴M. David, A. Toutant, and F. Bataille, "Direct simulations and subgrid modeling of turbulent channel flows asymmetrically heated from both walls," *Physics of Fluids* **33**, 085111 (2021).
- ⁴⁵M. David, A. Toutant, and F. Bataille, "Investigation of thermal large-eddy simulation approaches in a highly turbulent channel flow submitted to strong asymmetric heating," *Physics of Fluids* **33**, 045104 (2021).
- ⁴⁶S. Hoyas and J. Jiménez, "Scaling of the velocity fluctuations in turbulent channels up to $Re_\tau=2003$," *Physics of Fluids* **18**, 011702 (2006).
- ⁴⁷J. Boussinesq, *Essai sur la théorie des eaux courantes* (Impr. nationale, 1877).
- ⁴⁸M. Lesieur, "Large-Eddy Simulations," in *Turbulence in Fluids*, Fluid Mechanics and Its Applications, edited by M. Lesieur (Springer Netherlands, Dordrecht, 1997) pp. 375–408.
- ⁴⁹M. David, A. Toutant, and F. Bataille, "Study of asymmetrically heated flows passing through gas-pressurized solar receivers using Direct Numerical Simulations," *International Journal of Heat and Mass Transfer* **201**, 123577 (2023).
- ⁵⁰R. A. Clark, J. H. Ferziger, and W. C. Reynolds, "Evaluation of subgrid-scale models using an accurately simulated turbulent flow," *Journal of Fluid Mechanics* **91**, 1–16 (1979).
- ⁵¹J. Bardina, J. Ferziger, and W. Reynolds, "Improved subgrid-scale models for large-eddy simulation," in *13th Fluid and Plasma Dynamics Conference, Fluid Dynamics and Co-located Conferences* (American Institute of Aeronautics and Astronautics, 1980).
- ⁵²S. Liu, C. Meneveau, and J. Katz, "On the properties of similarity subgrid-scale models as deduced from measurements in a turbulent jet," *Journal of Fluid Mechanics* **275**, 83–119 (1994).
- ⁵³P. Sagaut, *Large Eddy Simulation for Incompressible Flows*, 3rd ed. (Springer, 1998).
- ⁵⁴R. Akhavan, A. Ansari, S. Kang, and N. Mangiavacchi, "Subgrid-scale interactions in a numerically simulated planar turbulent jet and implications for modelling," *Journal of Fluid Mechanics* **408**, 83–120 (2000).
- ⁵⁵C. Meneveau and J. Katz, "Conditional subgrid force and dissipation in locally isotropic and rapidly strained turbulence," *Physics of Fluids* **11**, 2317–2329 (1999).
- ⁵⁶U. Piomelli, G. N. Coleman, and J. Kim, "On the effects of nonequilibrium on the subgrid-scale stresses," *Physics of Fluids* **9**, 2740–2748 (1997).
- ⁵⁷G. S. Winckelmans, H. Jeanmart, and D. Carati, "On the comparison of turbulence intensities from large-eddy simulation with those from experiment

This is the author's peer reviewed, accepted manuscript. However, the online version of record will be different from this version once it has been copyedited and typeset.

PLEASE CITE THIS ARTICLE AS DOI: 10.1063/5.0139433

- or direct numerical simulation," *Physics of Fluids* **14**, 1809–1811 (2002).
- ⁵⁸S.-G. Cai and P. Sagaut, "Explicit wall models for large eddy simulation," *Physics of Fluids* **33**, 041703 (2021).
- ⁵⁹D. Oberle, C. D. Pruett, and P. Jenny, "Temporal large-eddy simulation based on direct deconvolution," *Physics of Fluids* **32**, 065112 (2020).
- ⁶⁰J. Meyers and P. Sagaut, "Is plane-channel flow a friendly case for the testing of large-eddy simulation subgrid-scale models?" *Physics of Fluids* **19**, 048105 (2007).
- ⁶¹S. Rezaeiravesh and M. Liefvendahl, "Effect of grid resolution on large eddy simulation of wall-bounded turbulence," *Physics of Fluids* **30** (2018).
- ⁶²N. Hutchins and I. Marusic, "Large-scale influences in near-wall turbulence," *Philosophical Transactions of the Royal Society A: Mathematical, Physical and Engineering Sciences* **365**, 647–664 (2007).
- ⁶³L. Agostini and M. A. Leschziner, "On the influence of outer large-scale structures on near-wall turbulence in channel flow," *Physics of Fluids* **26**, 075107 (2014).
- ⁶⁴M. David, A. Toutant, and F. Bataille, "Impact of asymmetrical heating on the uncertainty propagation of flow parameters on wall heat transfers in solar receivers," *Applied Thermal Engineering* **199**, 117547 (2021).
- ⁶⁵C.-H. Moeng and J. C. Wyngaard, "Spectral Analysis of Large-Eddy Simulations of the Convective Boundary Layer," *Journal of the Atmospheric Sciences* **45**, 3573–3587 (1988).
- ⁶⁶J. Boudet, J. Caro, L. Shao, and E. L  v  que, "Numerical studies towards practical large-eddy simulation," *Journal of Thermal Science* **16**, 328–336 (2007).